

Supplementary Material

1 SUPPLEMENTARY METHODS: MODEL WORKFLOW AND SOLVER APPROACHES

Figure S1 shows a schematic layout of the coupled model workflow. The 1D conduit, vent/MWI, and plume models are each solved in series (conduit output at $z = 0$ becomes vent model input, and vent model output at $z = Z_e$ becomes plume model input) using a variable-step, stiff differential equation solver in MATLAB, ode15s. The conduit model code is directly from Hajimirza et al. (2021), with minor modifications to allow the ambient surface pressure boundary condition to be determined based on a specified water depth. The plume model also uses existing code from Degruyter and Bonadonna (2012), with minor modifications from Aubry and Jellinek (2018). We have further modified the plume code to incorporate the particle fallout scheme of Girault et al. (2014), and the resulting system of differential equations are shown in Equations (53)-(58).

The vent/MWI model consists of two components, which run in series: 1) vent decompression and 2) water entrainment. The decompression model estimates the velocity, density, and radius, and related parameters (e.g. bulk modulus, gas volume fraction, and mixture sound speed) of the erupting jet following decompression to ambient pressure (as a function of water depth). The above estimated jet parameters following decompression then become the starting conditions at $z = L_d$ for the water entrainment model. The calculation for parameters following gas expansion at $z = L_d$ proceeds in two steps. (1) The decompression length L_d is estimated according to Equations 13 through 16, using ambient pressure at $z = 0$. (2) The jet parameters (density, radius, velocity) are recalculated using ambient pressure at $z = L_d$. This second step assumes the jet is pressure balanced (and thus allows entrainment to begin in our model) at $z = L_d$. However, because the jet continually decompresses above the vent owing to the significant change in ambient pressure with height in the water column, this estimate of L_d is likely a lower bound. This low bound is preferred, however, as it provides a relatively conservative estimate for the height at which turbulent entrainment is likely to begin. In cases where the estimated L_d is greater than the water depth, the jet parameters are calculated assuming atmospheric ambient density, and the plume model is initialized directly. By design, this assumes negligible incorporation of water into the jet for $L_d \geq Z_e$, as noted in Section 2.3.2.

2 THERMAL STRESS FROM QUENCHING, GLASS TRANSITION TEMPERATURE, AND FRAGMENTATION ENERGY EFFICIENCY

Here we highlight the rationale for the temperature dependent fragmentation efficiency of Section 2.3.4 (in particular Equations 42-43). Moitra et al. (2020) estimate the thermal stress σ_T generated at the surface of a cooling pyroclast that is insulated from surrounding liquid water by a continuous film of water vapor (Kingery, 1955; Strobl et al., 2018). Accounting for the heat transfer properties of the hot pyroclast and vapor film in series through a standard Biot number Bi approach, they find:

$$\sigma_T = \frac{Y}{1 - \nu} \alpha_T \Delta T \left(1 + \frac{5}{Bi} - \frac{1.897}{Bi^{1/2}} + \frac{9.119}{Bi^{1/3}} - \frac{8.540}{Bi^{1/4}} + \frac{2.989}{Bi^{1/5}} \right), \quad (S1)$$

where Y is the pyroclast Young's modulus, ν is Poisson's ratio, and $\Delta T = T - T_{sat}$ is the temperature difference between the particle interior and the boiling water-pyroclast interface. The coefficient of thermal

expansion α_T has approximately constant values below and above the glass transition of $\alpha_{T,glass} \approx 2 \times 10^{-5} \text{ K}^{-1}$ and $\alpha_{T,liq} \approx 7 \times 10^{-5} \text{ K}^{-1}$, respectively (Bouhifd et al., 2015). Here we approximate α_T using the smooth heaviside step function of Equation 42:

$$\alpha_T = (\alpha_{T,liq} - \alpha_{T,glass}) \left\{ 1 + \exp \left[\frac{-6}{\Delta T_g} \left(T - \left(T_g + \frac{\Delta T_g}{2} \right) \right) \right] \right\}^{-1} + \alpha_{T,glass}. \quad (\text{S2})$$

Here, the Biot Number Bi expresses the relative resistances of the solid and film to the diffusion of heat and is given by:

$$Bi = \frac{hl}{\rho_s C_s d_T}. \quad (\text{S3})$$

Here, h is the heat transfer coefficient for the film, l is the characteristic diffusion length scale over which thermal stresses are generated in the pyroclast, and the thermal diffusivity d_T is (Moitra et al., 2018):

$$d_T = \begin{cases} 5.98T^{-0.41} + (9.23 \times 10^{-5})T & T < T_g \\ 0.06 + (4.57 \times 10^{-4})T & T \geq T_g. \end{cases} \quad (\text{S4})$$

Calculated values for Equations S1-S4 are shown in Figure S4 using values equivalent to those of Moitra et al. (2020). We use three length scales corresponding to the mean, upper, and lower bounds of the hydrovolcanic PSD used in this study (phi size units, $\phi = 3.43 \pm 1.46$, see Section 2.3.4). Thermal stresses easily exceed yield stresses above the glass transition over length scales corresponding to the mean diameter of particles following quench fragmentation. Yield stress limits are less readily exceeded (though still possible) below the glass transition. Note that yield stresses shown in Figure S4d and reported in Heap et al. (2014) are for compressive failure stresses and therefore likely upper bounds. The various parameters used here, particularly the Young's modulus, heat transfer coefficient, and yield stress, may take a large range of values depending on particle shape and size, porosity, flow regime, and the presence and stability of boiling vapor films. The large change in estimated thermal stress in Equation S1, however, is dominated by the relatively step-wise change in α_T . This suggests that to a leading order, the PSD is primarily modified by quench fragmentation processes while particles are cooled across the glass transition, and than this process is relatively much less efficient once internal particle temperatures pass below this threshold. Following the above discussion, we adopt the simple fragmentation energy efficiency scheme outlined in Section 2.3.4, which accounts for the irreversible energy losses of fragmentation and is guided by the experimental relationship of Sonder et al. (2011), with an assumed falloff in fragmentation below the glass transition given by Equations 42 and 43.

3 COMPARISON OF THEORETICAL VENT CHOKING CONDITIONS WITH CONDUIT MODEL RESULTS

Here we compare the results of our existing model scenarios, in which no external water accesses the conduit, with simple theoretical relationships for conduit MER, sound speed, and vent pressure, based on Woods and Bower (1995); Koyaguchi (2005); Koyaguchi et al. (2010). Modeled vent pressure for the *Reference* scenario is compared against Equation 59 in Figure S6, with points colored by external water depth. The agreement is excellent for choked vent simulations (filled circles), whereas simulations in which hydrostatic pressure exceeds P_{choke} are pressure-balanced ($\beta \approx 1$, $M < 1$) at the vent (open circles).

Figure S7 shows vent overpressure β as a function of water depth (normalized to conduit radius). Simulated values from the *Reference* scenario are shown with circles, where filled circles represent choked

vents (colored by initial magmatic gas fraction n_0) and open gray circles are pressure balance vents. Colored lines show values of β estimated using Equations 59 and 61 for varying n_{ec} . These results demonstrate that as water infiltrates into the conduit in increasing max fractions, the external water depth limit for choking increases from about 5 vent radii at typical magmatic gas mass fractions of $n \approx 0.03$ to about 10 vent radii for $n_{ec} = 0.15$ ($n \approx 0.18$). The difference between the theoretical calculation and simulation results at high overpressure results from differences in the sound speed formulation, as highlighted by the black dashed line which shows the result using sound speed from Equation 6 (as compared to Equation 59) and with no external water.

REFERENCES

- Aubry, T. J. and Jellinek, A. M. (2018). New insights on entrainment and condensation in volcanic plumes: Constraints from independent observations of explosive eruptions and implications for assessing their impacts. *Earth and Planetary Science Letters* 490, 132–142. doi:10.1016/j.epsl.2018.03.028
- Aubry, T. J., Staunton-Sykes, J., Marshall, L. R., Haywood, J., Abraham, N. L., and Schmidt, A. (2021). Climate change modulates the stratospheric volcanic sulfate aerosol lifecycle and radiative forcing from tropical eruptions. *Nature Communications* 12, 4708. doi:10.1038/s41467-021-24943-7
- Bouhifd, M. A., Whittington, A. G., and Richet, P. (2015). Densities and volumes of hydrous silicate melts: New measurements and predictions. *Chemical Geology* 418, 40–50. doi:10.1016/j.chemgeo.2015.01.012
- Costa, A., Pioli, L., and Bonadonna, C. (2016). Assessing tephra total grain-size distribution: Insights from field data analysis. *Earth and Planetary Science Letters* 443, 90–107. doi:10.1016/j.epsl.2016.02.040
- Degruyter, W. and Bonadonna, C. (2012). Improving on mass flow rate estimates of volcanic eruptions. *Geophysical Research Letters* 39. doi:10.1029/2012GL052566
- Girault, F., Carazzo, G., Tait, S., Ferrucci, F., and Kaminski, É. (2014). The effect of total grain-size distribution on the dynamics of turbulent volcanic plumes. *Earth and Planetary Science Letters* 394, 124–134. doi:10.1016/j.epsl.2014.03.021
- Hajimirza, S., Gonnermann, H. M., and Gardner, J. E. (2021). Reconciling bubble nucleation in explosive eruptions with geospeedometers. *Nature Communications* 12, 283. doi:10.1038/s41467-020-20541-1
- Heap, M. J., Xu, T., and Chen, C.-f. (2014). The influence of porosity and vesicle size on the brittle strength of volcanic rocks and magma. *Bulletin of Volcanology* 76, 856. doi:10.1007/s00445-014-0856-0
- Hersbach, H., Bell, B., Berrisford, P., Hirahara, S., Horányi, A., Muñoz-Sabater, J., et al. (2020). The ERA5 global reanalysis. *Quarterly Journal of the Royal Meteorological Society* 146, 1999–2049. doi:10.1002/qj.3803
- Kingery, W. D. (1955). Factors Affecting Thermal Stress Resistance of Ceramic Materials. *Journal of the American Ceramic Society* 38, 3–15. doi:10.1111/j.1151-2916.1955.tb14545.x
- Koyaguchi, T. (2005). An analytical study for 1-dimensional steady flow in volcanic conduits. *Journal of Volcanology and Geothermal Research* 143, 29–52. doi:10.1016/j.jvolgeores.2004.09.009
- Koyaguchi, T., Suzuki, Y. J., and Kozono, T. (2010). Effects of the crater on eruption column dynamics. *Journal of Geophysical Research: Solid Earth* 115. doi:10.1029/2009JB007146
- Moitra, P., Sonder, I., and Valentine, G. A. (2018). Effects of Size and Temperature-Dependent Thermal Conductivity on the Cooling of Pyroclasts in Air. *Geochemistry, Geophysics, Geosystems* 19, 3623–3636. doi:10.1029/2018GC007510
- Moitra, P., Sonder, I., and Valentine, G. A. (2020). The role of external water on rapid cooling and fragmentation of magma. *Earth and Planetary Science Letters* 537, 116194. doi:10.1016/j.epsl.2020.116194

- Ogden, D. E., Wohletz, K. H., Glatzmaier, G. A., and Brodsky, E. E. (2008). Numerical simulations of volcanic jets: Importance of vent overpressure. *Journal of Geophysical Research: Solid Earth* 113, B02204. doi:10.1029/2007JB005133
- Sonder, I., Schmid, A., Seegelken, R., Zimanowski, B., and Büttner, R. (2011). Heat source or heat sink: What dominates behavior of non-explosive magma-water interaction? *Journal of Geophysical Research: Solid Earth* 116. doi:10.1029/2011JB008280
- Strobl, S., Adlmann, F.-A., Supancic, P., Lube, T., Danzer, R., and Schöppl, O. (2018). Fracture toughness of silicon nitride balls via thermal shock. *Journal of the European Ceramic Society* 38, 1278–1287. doi:10.1016/j.jeurceramsoc.2017.11.005
- Woods, A. W. and Bower, S. M. (1995). The decompression of volcanic jets in a crater during explosive volcanic eruptions. *Earth and Planetary Science Letters* 131, 189–205. doi:10.1016/0012-821X(95)00012-2

4 SUPPLEMENTARY FIGURES

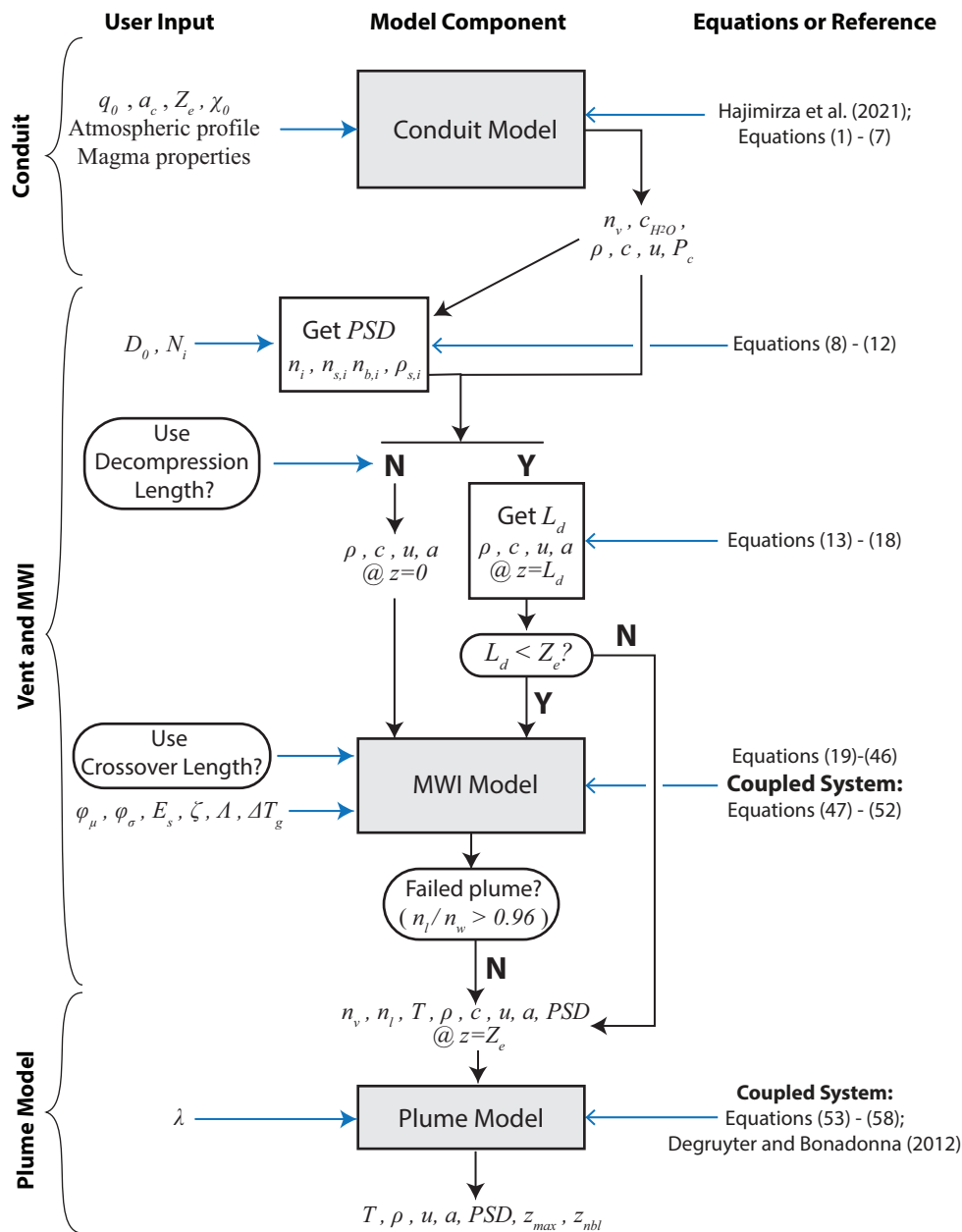


Figure S1. Coupled model workflow, showing the main user input parameters for each step and relevant equations from the main text. Primary model components involving integration of differential equations are shaded in gray.

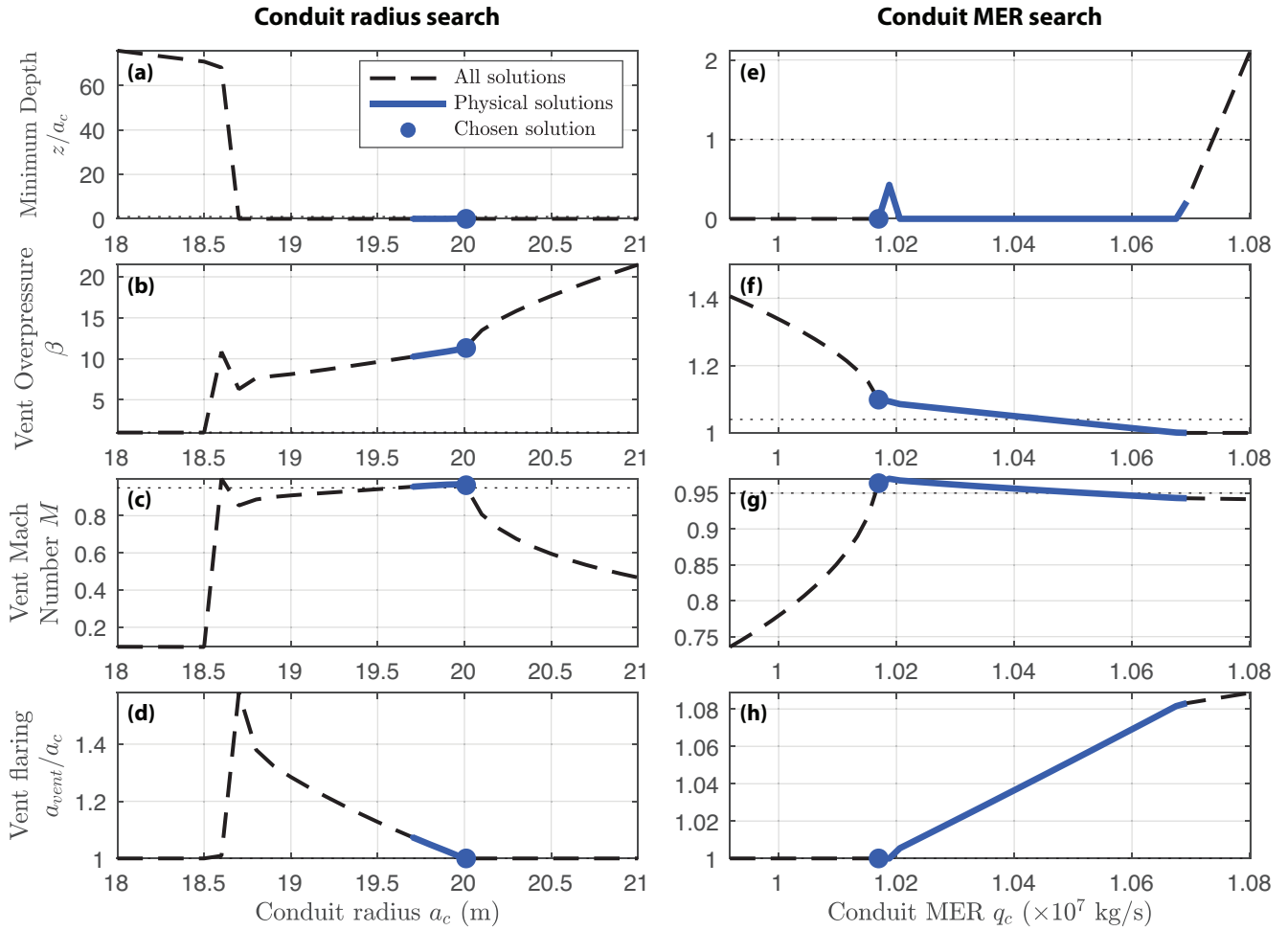


Figure S2. Conduit model solution search for control MER $Q_0 = 10^7$ kg/s. It is possible to obtain conduit model solutions that integrate successfully but are non-physical. Accordingly, we search for valid solutions first with fixed control MER Q_0 , varying conduit radius a_c for subaerial control simulations (panels (a)-(d)), then search across varying adjusted MER q_c for hydrovolcanic simulations (panels (e)-(h)). (a) Minimum depth. Flow does not reach the surface in some simulations, usually because either conduit pressure or velocity decrease to zero. Accordingly, we require physical solutions that reach depths less than about 1 conduit radius below the vent. (b) Vent overpressure ratio β . (c) Vent Mach Number M . Physical solutions must be either choked ($M \gtrsim 0.95$) and overpressured ($\beta \gtrsim 1.04$) or pressure balanced ($\beta \approx 1$) and subsonic ($M < 1$). (d) Vent flaring (ratio of vent radius to conduit radius). Amongst physically valid solutions, we choose the solution that minimizes vent flaring (blue circles). (e)-(h) are as for (a)-(d), but searching across variable MER for fixed radius and water depth $Z_e = 100m$.

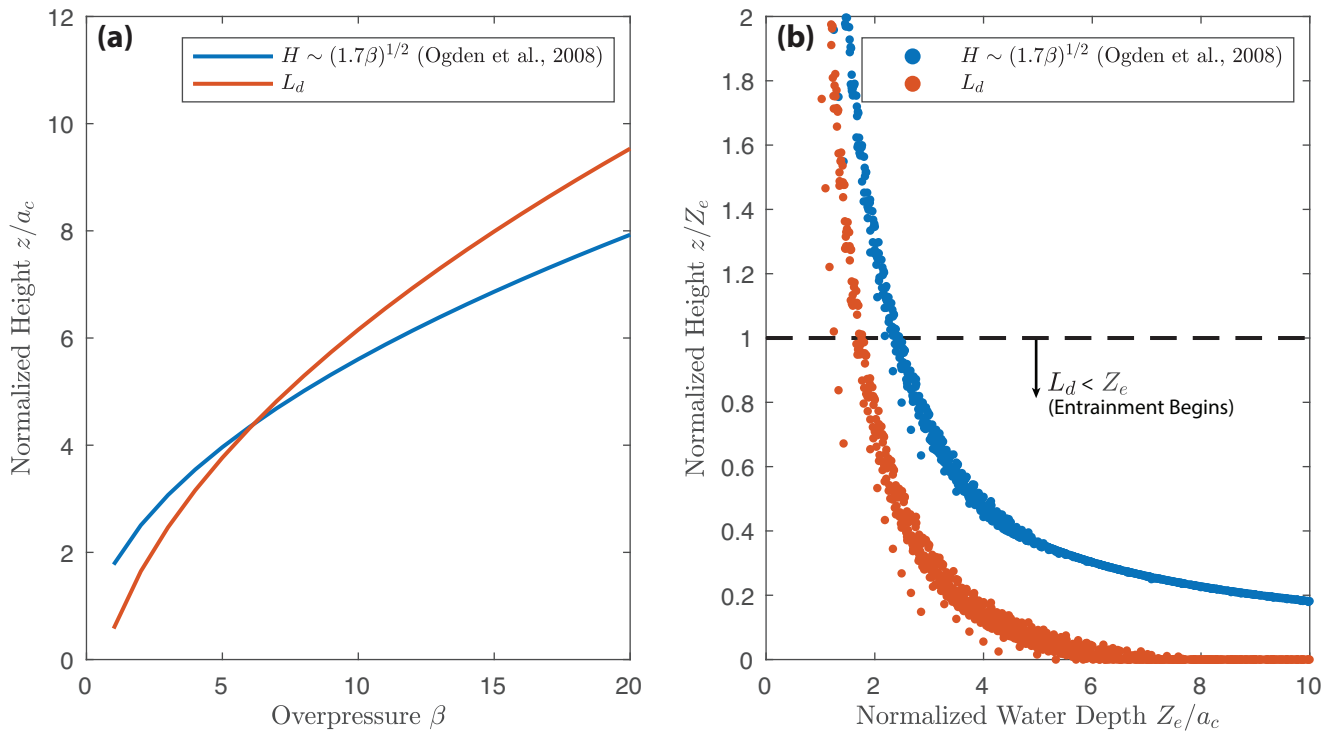


Figure S3. Decompression length L_d as compared with the Mach disk height scaling of Ogden et al. (2008). (a) Mach disk height and decompression length L_d normalized to conduit radius a_c as a function of vent overpressure ratio β . (b) Mach disk height and decompression length L_d normalized to external water depth Z_e , as a function of water depth normalized to conduit radius a_c for simulations in the *Reference* scenario. The formal definition of L_d as the height at which entrainment by turbulent mechanisms can begin requires that $L_d \rightarrow 0$ as $\beta \rightarrow 1$.

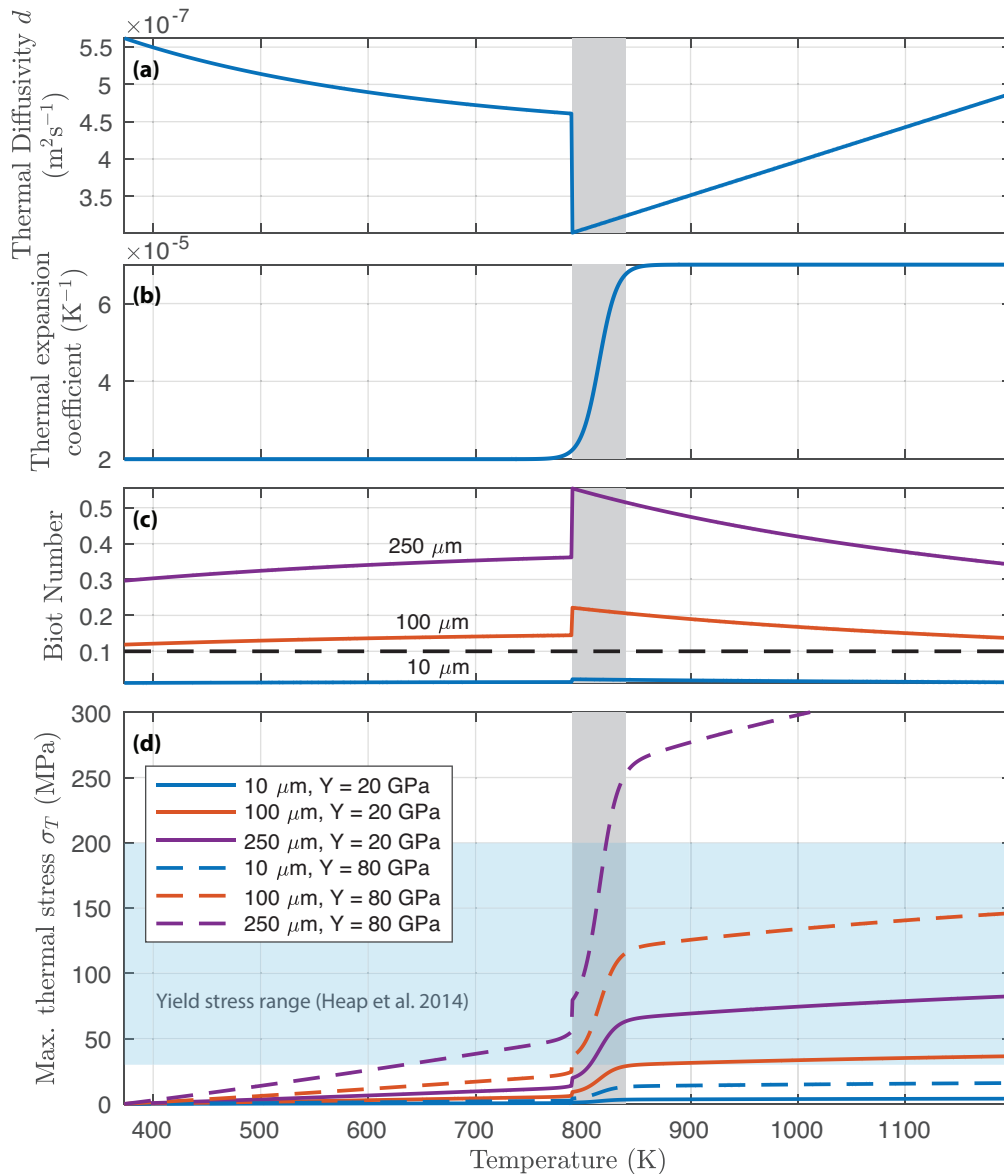


Figure S4. Theoretical thermal shock stress on quenching pyroclasts as a function of temperature difference and particle length scale following Equation S1. The glass transition temperature range is marked with a gray shaded area in all panels. (a) Thermal diffusivity α_T from Equation S4 Moitra et al. (2018). (b) Thermal expansion coefficient from Equation S2, with values above and below the glass transition obtained from Bouhifd et al. (2015). (c) Biot number for three particle sizes corresponding approximately to the particle size range (ϕ size units, $\phi = 3.43 \pm 1.46$) for the Askja Phase C deposit (Costa et al., 2016). The critical Biot number of 0.1 above which Equation S1 is expected to be valid (Moitra et al., 2018) is marked with the black dashed line. (d) Maximum thermal stress from Equation S1 for the three particle sizes of panel (c) and assuming two different elastic moduli. $Y = 80$ GPa is appropriate for solid glass, whereas 20 GPa corresponds to a vesicular glass (Heap et al., 2014). Approximate range of (compressive) yield stresses from Heap et al. (2014) is shown by the blue shaded region.

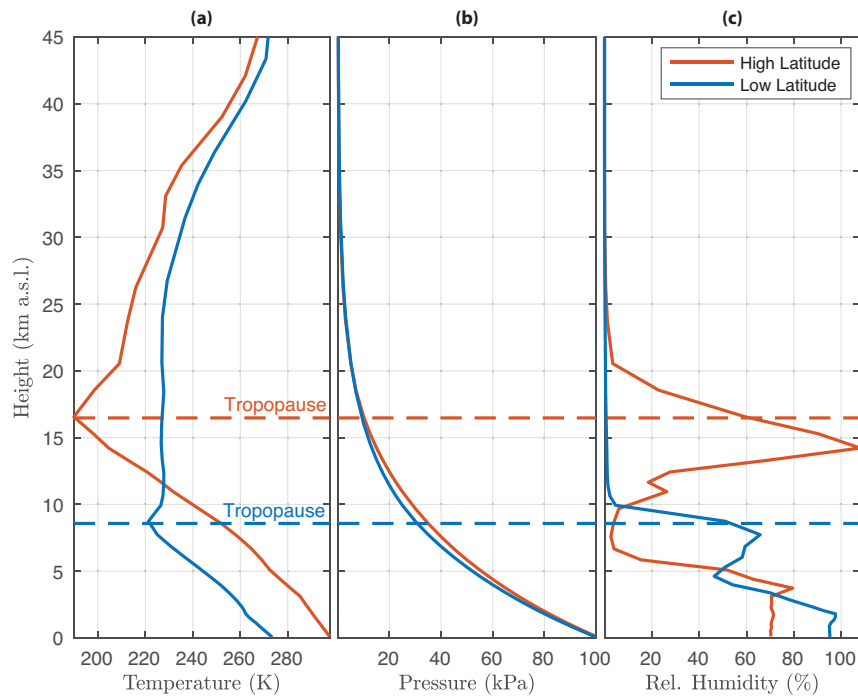


Figure S5. Atmospheric profiles used in the simulation scenarios, obtained from ERA reanalysis data (Hersbach et al., 2020; Aubry et al., 2021). (a) Temperature, (b) pressure, (c) relative humidity. The high-latitude atmospheric profile used in all scenarios except *Low-Lat* is that from the 2011 eruption of Grímsvötn Volcano, with a corresponding vent altitude of 1750 m a.s.l. For the *Low-Lat* scenario, we use the atmospheric profile for the 2014 eruption of Tungurahua Volcano with vent altitude 0 m a.s.l.

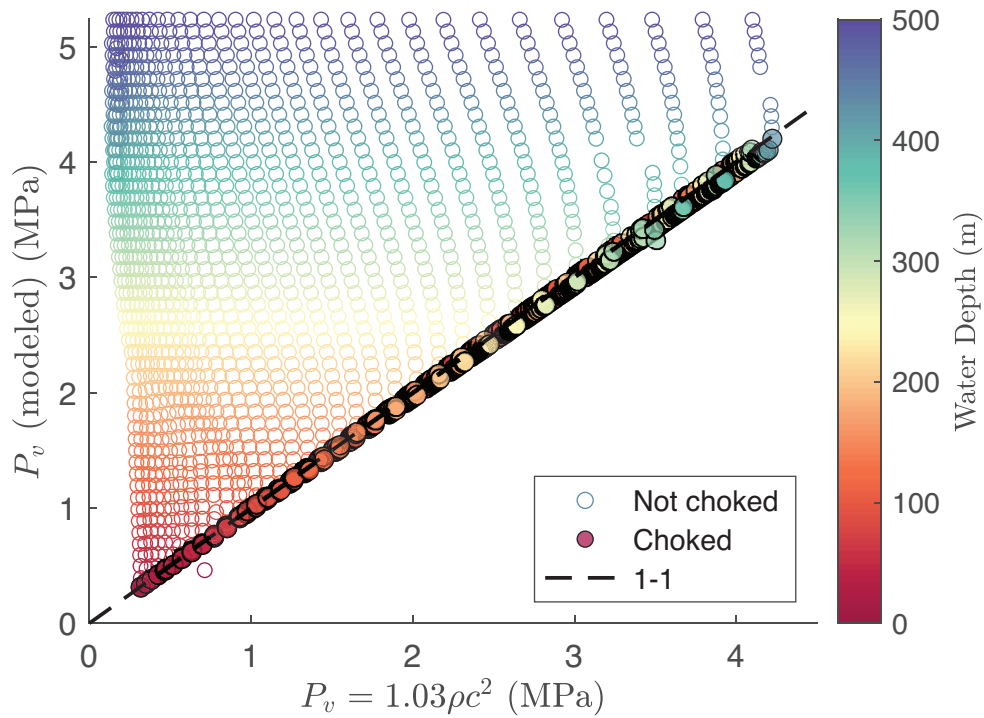


Figure S6. Modeled vent pressure versus theoretical choked vent pressure, following Koyaguchi (2005). Simulations where external hydrostatic pressure exceeds the choking pressure are shown in open circles, while simulations where the vent pressure matches the choking condition are shown with filled circles. The scale factor of $1.03 = 1/0.97$ on the x-axis results from the fact that vent velocity in the conduit model is typically limited to about $M = 0.97$, since $M = 1$ results in a singularity in Equation 5.

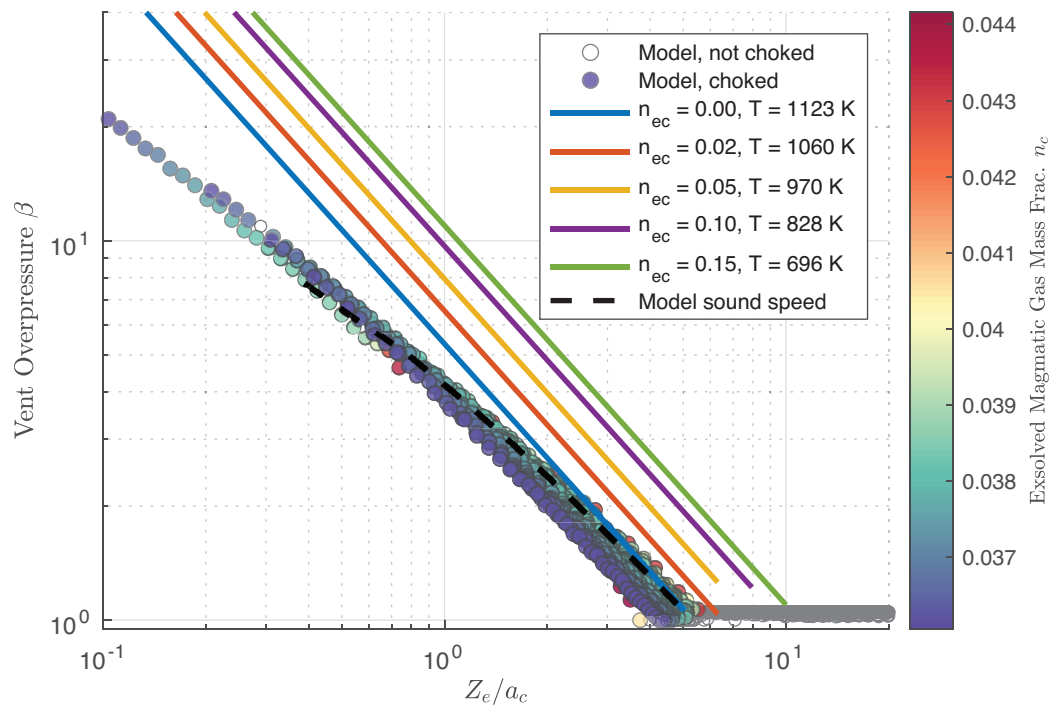


Figure S7. Vent overpressure β versus water depth (normalized to vent radius). Model results of the *Reference* scenario are shown in circles (filled circles for choked vents, open circles for pressure-balanced jets). Theoretical relationships for β as a function of mass fraction of external water infiltrated into the conduit are shown in solid lines. The difference between modeled and theoretical results at high overpressures results from different formulations for sound speed.